Testing meson portal dark sector solutions to the MiniBooNE anomaly at the Coherent CAPTAIN Mills experiment

A. A. Aguilar-Arevalo,[8] S. Biedron,[9] J. Boissevain,[1] M. Borrego,[6] L. Bugel,[7] M. Chavez-Estrada,[8] J. M. Conrad,[7] R. L. Cooper,[6,10] A. Diaz,[7] J. R. Distel,[6] J. C. D'Olivo,[8] E. Dunton,[2] B. Dutta,[11] D. Fields,[9] J. R. Gochanour,[6] M. Gold,[9] E. Guardincerri,[6] E. C. Huang,[6] N. Kamp,[7] D. Kim,[11] K. Knickerbocker,[6] W. C. Louis,[6] J. T. M. Lyles,[6] R. Mahapatra,[11] S. Maludze,[11] J. Mirabal,[6] D. Newmark,[7] P. deNiverville,[6] V. Pandey,[5] D. Poulson,[6] H. Ray,[5] E. Renner,[6] T. J. Schaub,[9] A. Schneider,[7] M. H. Shaevitz,[2] D. Smith,[4] W. Sondheim,[6] A. M. Szelc,[3] C. Taylor,[6] A. Thompson,[12] W. H. Thompson,[6] M. Tripathi,[5] R. T. Thornton,[6] R. Van Berg,[1] and R. G. Van de Water[6]

[1]*Bartoszek Engineering, Aurora, Illinois 60506, USA*
[2]*Columbia University, New York, New York 10027, USA*
[3]*University of Edinburgh, Edinburgh, United Kingdom*
[4]*Embry–Riddle Aeronautical University, Prescott, Arizona 86301, USA*
[5]*University of Florida, Gainesville, Florida 32611, USA*
[6]*Los Alamos National Laboratory, Los Alamos, New Mexico 87545, USA*
[7]*Massachusetts Institute of Technology, Cambridge, Massachusetts 02139, USA*
[8]*Universidad Nacional Autónoma de México, CDMX 04510, Mexico*
[9]*University of New Mexico, Albuquerque, New Mexico 87131, USA*
[10]*New Mexico State University, Las Cruces, New Mexico 88003, USA*
[11]*Texas A&M University, College Station, Texas 77843, USA*
[12]*Northwestern University, Evanston, Illinois 60208, USA*

(Received 10 October 2023; accepted 21 April 2024; published 13 May 2024)

A solution to the MiniBooNE excess invoking rare three-body decays of the charged pions and kaons to new states in the MeV mass scale was recently proposed as a dark-sector explanation. This class of solution illuminates the fact that, while the charged pions were focused in the target-mode run, their decay products were isotropically suppressed in the beam-dump-mode run in which no excess was observed. This suggests a new physics solution correlated to the mesonic sector. We investigate an extended set of phenomenological models that can explain the MiniBooNE excess as a dark sector solution, utilizing long-lived particles that might be produced in the three-body decays of the charged mesons and the two-body anomalous decays of the neutral mesons. Over a broad set of interactions with the long-lived particles, we show that these scenarios can be compatible with constraints from LSND, KARMEN, and MicroBooNE, and evaluate the sensitivity of the ongoing and future data taken by the Coherent CAPTAIN Mills experiment to a potential discovery in this parameter space.

DOI: 10.1103/PhysRevD.109.095017

I. INTRODUCTION

The excess of electronlike events observed by MiniBooNE [1–3] at a level of 4.8σ has remained one of the stronger hints to the existence of new physics beyond the Standard Model (BSM). The event data observed in the MiniBooNE detector is remarkable for its spectrum, with the excess appearing at forward scattering angles ($\cos\theta > 0.75$) and low energies ($E_{\rm vis} < 500$ MeV), and for the asymmetry of excess events in the neutrino and antineutrino modes, while no excess was observed in the dump mode [4], which had a reduced neutrino flux.

Neutrino-based new physics explanations have been popular solutions to the anomaly [5–42]. Since the neutrinos at MiniBooNE are produced primarily from charged meson decays and the decays of daughter muons of those charged mesons, neutrino-based solutions can accommodate the absence of any excess in the dump mode, in which the charged mesons are no longer focused by magnetic horns, unlike the neutrino and antineutrino modes. Essentially, the neutrino-based explanations work well because a key feature of the excess seems to be correlated to the focusing or suppression of charged mesons. Further, since the energy and angular distributions of the excess are already characteristic of neutrinolike signals and backgrounds, new physics appearing in the neutrino sector may naturally map onto the observed spectra.

This poses a challenge to dark sector interpretations of the excess (e.g., using π^0 or dark bremsstrahlung production channels [4,43]), which have been more constrained and less complete in their explanation of the excess with respect to their counterparts in neutrino BSM physics thus far. Recently, a generic set of solutions to the excess was proposed in Ref. [44] using a framework of rare three-body decays of the charged mesons—decays which may not be strongly suppressed in their phase space and can be powerful probes of BSM physics [45–50]. One subset of models considered consists of a long-lived dark sector boson [not necessarily the cosmological dark matter, but at least long-lived on the scale of the baseline from the Booster Neutrino Beam (BNB) to the MiniBooNE detector of ∼500 m] that can survive and scatter in the MiniBooNE detector via a photoconversion process, leaving a single photon in the final state. Since the Cherenkov detector does not distinguish between photons and electrons, this scattering process can be a viable contributor to the excess, provided that the appropriate phenomenological model can be found to be safe from existing constraints.

In this work, we will constrain the space of operators in an effective field theory (EFT) that leads to rare three-body decays of the charged mesons and photoconversion scattering of long-lived mediators at Coherent CAPTAIN Mills (CCM), utilizing the close proximity to the Lujan beam target as a source of stopped-pion decays. Using the CCM120 engineering run, we set conservative limits on the parameter space, and forecast sensitivity for the ongoing three-year run with the upgraded CCM200 detector. A similar analysis for electromagnetic signal region of interest that was performed for axionlike particles in Ref. [51] is carried out here. In surveying the greater landscape of dark sector models that can explain the MiniBooNE anomaly via rare meson decays, we also take into account the analyses and observations from other stopped-pion experiments like LSND and KARMEN. Important findings about the parameter space that we consider here can be distilled from the existing data at MicroBooNE, and other forthcoming short-baseline experiments like SBND have a discovery potential here as we will show. In fact, the joint analysis of close-proximity stopped-pion experiments and those at the short-baseline neutrino program with magnetic horn-focused charged meson fluxes will have total experimental coverage over the parameter space explaining the anomaly.

This paper is organized as follows. In Sec. II we introduce the operator EFT extension to the SM that we wish to consider and connect it to a phenomenological model of pion decays and photoconversion scattering in Sec. III. In Sec. IV the analysis procedures for both MiniBooNE target and dump mode runs is discussed, in addition to our analysis of LSND, KARMEN, and MicroBooNE data interpreted as constraints on the models in question. In Sec. V we show the analysis procedure for the CCM120 engineering run data and construct forecasts for the ongoing CCM200 data-taking run. In Sec. VI the resulting fits and constraints are shown for several benchmark models that utilize the operators we have considered in Sec. II, and finally in Sec. VII we conclude.

II. MODELS

We study a set of effective operators which permit, at a purely phenomenological level, the production of a long-lived particle (LLP) bosonic state from the three-body decay of the charged mesons, and subsequent photoconversion of said meson via a massive mediator; schematically,

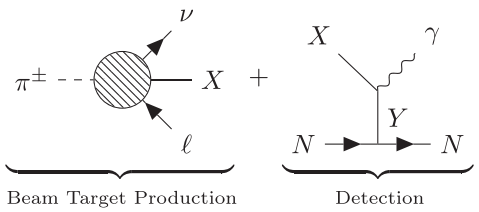

This simple setup was shown to explain the MiniBooNE excess in Ref. [44], making use of two prominent features; (I) the coupling of a boson X to the charged pion decays ensures the X flux is correlated to the relative size of the excess in the target and off-target modes through the focusing of charged pions via the magnetic horns, and (II) the mass of the mediator Y gives a dial to tune the angular spectrum of the outgoing γ's Cherenkov ring, which is characteristically off forward.

We will investigate a broad set of operators that allow for such a phenomenology in order to estimate the relative sizes of the parameter space allowed by existing constraints that also can accommodate the MiniBooNE excess. In Sec. II A we consider a generic EFT for the two bosons X and Y below the QCD scale, while in Sec. II B we consider a hadrophillic scenario, with a single new boson whose dominant couplings are to the first generation of quarks, and connect the EFT to specific quark couplings above the QCD scale.

A. One long-lived boson and a secondary massive mediator

We study two BSM scenarios that each could explain the MiniBooNE excess and are testable at stopped pion and other beam dump facilities. In the first scenario, we extend the low energy SM EFT with two massive bosons, one of them long-lived and being produced via the three-body decay of the charged mesons and the other generally being heavier and facilitating photoconversion $XN \to \gamma N$. These decay and scattering mechanisms can arise from a multitude of operators. For the decays, scalars (ϕ), pseudoscalars (a), or vectors (V) coupled to the electrons or muons through $g^s_\ell \phi \bar{\ell}\ell$, $-ig^p_\ell a \bar{\ell}\gamma^5\ell$, and $g^V_\ell V_\mu \bar{\ell}\gamma^\mu\ell$ terms allow for $\pi^\pm \to X\ell\nu$ where $X = \phi, a, V$ is radiated off the charged lepton leg. Alternatively, effective couplings to the charged pions through operators like $g^s_\pi \phi\pi^+\pi^-$ or $g^v_\pi V_\mu \pi^+(\partial^\mu\pi^-)$

allow for radiative decays from the pion current (and potentially other contact and pion structure-dependent interactions, discussed in the next section).

On the detection side, the long-lived ϕ, a, or V mediators can induce single-photon final states through the dimension-5 couplings $\frac{\lambda^s}{4}\phi H_{\mu\nu}F^{\mu\nu}$ and $\frac{\lambda^p}{4}aH_{\mu\nu}\tilde{F}^{\mu\nu}$, where we define $H_{\mu\nu} \equiv \partial_\mu V_\nu - \partial_\nu V_\mu$. In these cases, either a vector, scalar, or pseudoscalar can serve as the long-lived X and another as the scattering mediator Y. Such operators can arise easily in concrete, UV-complete models. For example, they can fit within the framework of a $U(1)$ extension to the SM with extra fermions that permit a loop-induced coupling between a (pseduo)scalar, the $U(1)$ gauge boson, and the SM photon [see, e.g., $U(1)_{T3R}$ [52] models or dark photon/axion portals [53]].

B. A single long-lived boson coupling to quarks

For this scenario, we consider a hadrophillic model that only couples to first generation quarks. Let us start with a massive vector boson, where above the QCD phase transition, its interactions with quarks is described by the Lagrangian

$$\mathcal{L} \supset \sum_{q=u,d} g_q V_\mu \bar{q}\gamma^\mu q + \text{H.c.} \tag{1}$$

We could interpret this as an extra $U(1)$ gauging the quarks with some dark charge, for example. Taking this below the QCD scale in the chiral perturbation theory (χPT), we have an operator like [54]

$$\mathcal{L}^{\chi\text{PT}} \supset i g_{\pi^\pm} V_\mu \pi^+ (\partial^\mu \pi^-). \tag{2}$$

Additionally, the chiral anomaly will lead to the anomalous decay of the π^0 to γV through the dimension-5 operator

$$\mathcal{L}^{\chi\text{PT}} \supset g_{\pi^0} \frac{e}{16\pi f_\pi} \pi^0 F_{\mu\nu}\tilde{H}^{\mu\nu}. \tag{3}$$

We have defined $H_{\alpha\beta} = \partial_\alpha V_\beta - \partial_\beta V_\alpha$, and $\tilde{H}^{\mu\nu} = \epsilon^{\mu\nu\alpha\beta}H_{\alpha\beta}$. The dimension-5 interaction $\sim\pi^0 F_{\mu\nu}\tilde{H}^{\mu\nu}$ permits $XN \to \gamma N$ via the pion-nucleon interaction $i g_{\pi N}\pi^0\bar{\psi}\gamma^5\psi$. This is an interaction of strong coupling; $g_{\pi N} \simeq 13$ [55].[1]

III. PHENOMENOLOGY

A. Three-body decays of charged mesons

The three-body radiative decay of the X boson off the pion current (Fig. 1) can be modeled off the work on radiative meson decays in the SM, like $\pi \to \gamma e\nu$ (see, for example, Refs. [56,57]). For the process $\pi(p) \to X(k)e(\ell)\nu(q)$, there

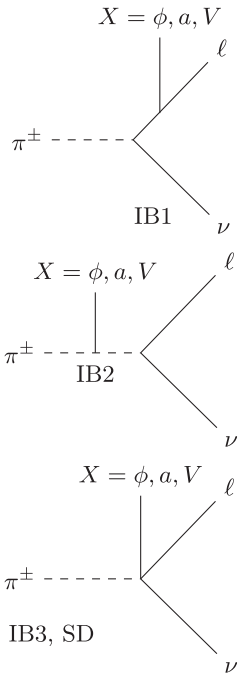

FIG. 1. Three-body charged meson decay $\pi \to \ell\nu X$ for a bosonic Lorentz representation $X = \phi, a, V$.

are several types of so-called "internal bremsstrahlung" (IB) interactions, adopting the nomenclature of the aforementioned reference; IB1, radiating X off the lepton leg; IB2, radiating off the charged meson current; and IB3, or a four-point contact interaction radiating off the pion-lepton vertex. Additionally, we may also consider structure-dependent (SD) terms originating from mixing between the new boson X and the vector mesons, but as these branching ratios are strongly suppressed, we will set them aside in this discussion.

Our discussion now focuses on a massive vector boson V taking part in these radiative decays, but we will return to the case of $X =$ scalar, pseudoscalar later.

The matrix elements for each process can be described by factorizing the leptonic and hadronic parts of the current:

$$\mathcal{M} = i\frac{G_F}{\sqrt{2}}\epsilon^\mu[\bar{u}_\ell\gamma^\rho(1-\gamma^5)v_\nu]T_{\mu\rho}, \tag{4}$$

where the hadronic tensor $T_{\mu\rho}$ can be expressed in terms of the amplitude,

$$T_{\mu\rho} = i\int d^4x e^{ikx}\langle 0|T[j^V_\mu(x)j^+_\rho(0)]|\pi^+(p)\rangle, \tag{5}$$

for currents $j^V_\mu = \sum_q g_q\bar{q}\gamma_\mu q$ and $j^+_\rho = \bar{d}\gamma_\rho(1-\gamma^5)u$. The IB2 term shown in Fig. 1, middle, is given by

$$T^{\text{IB2}}_{\mu\rho} = \frac{i(2p-k)_\mu(p-k)_\rho}{2p\cdot k - m_V^2} f_\pi \tag{6}$$

[1]One might also consider nuclear couplings which permit $VN \to VN$ scattering, leaving a nuclear recoil signature, but these processes would be $\mathcal{O}(g_q^4)$ suppressed.

which may come directly from the action in Eq. (2), $ig_{\pi^\pm}V_\mu\pi^+(\partial^\mu\pi^-)$, while additional contact and structure-dependent terms in Fig. 1, bottom, may come from less trivial interactions. For example, a simple contact term could manifest from making the gauge covariant replacement $\partial_\mu \to \partial_\mu - ig_{\pi^\pm}V_\mu$ in the pion-lepton Fermi interaction $(\partial_\mu\pi^+)\overline{\ell}\gamma^\mu(1-\gamma^5)\nu$.

However, we can only speculate about the gauge nature of our massive vector, and so to proceed naively we decompose the hadronic tensor $T_{\mu\rho}$ in a gauge covariant way. We follow the approach given in Ref. [58], expressing $T_{\mu\rho}$ in terms of the momenta k_μ and $L_\mu \equiv q_\mu + \ell_\mu$:

$$T_{\mu\rho} = \tilde{a}_0 g_{\mu\rho} + \tilde{b}_0 L_\mu k_\rho + \tilde{b}_1 L_\rho k_\mu + \tilde{b}_2 L_\mu L_\rho + \tilde{b}_3 k_\mu k_\rho + \epsilon_{\rho\mu\lambda\sigma}L^\lambda k^\sigma F_V, \quad (7)$$

where $\tilde{a}_0$, $\tilde{b}_i$ $(i = 0, 1, 2, 3)$, and F_V are dimensionful invariant amplitudes. For massless photons, satisfying the Ward identity imposes a relationship between the coefficients [58–61]. However, for a massive vector boson V^μ, no Ward identity needs to be satisfied in general, as a theory with massive vector bosons need not be gauge invariant. Noting that $L \cdot k = (p-k)\cdot k$, the IB2 term in Eq. (6) is recovered if one takes $\tilde{b}_2 = 2\tilde{b}_1 = if_\pi/(2L\cdot k + m_V^2)$. The remaining terms $\tilde{a}_0$, $\tilde{b}_0$, $\tilde{b}_2$, and F_V account for contact and structure dependent contributions. For example, a pure contact term would take the form

$$T^{\mathrm{IB3}}_{\mu\rho} = if_\pi\alpha g_{\mu\rho} + i\beta\frac{f_\pi}{(L\cdot k)}g_{\mu\rho} \quad (8)$$

for dimensionless constants α, β. In this analysis we will consider only two instances of the meson couplings; those of IB2 nature [Fig. 1, middle, or Eq. (6)] and those of a pure contact or IB3 nature [Fig. 1, bottom or Eq. (8)].

B. Dark boson photoconversion

Long-lived bosonic states may have dimension-5 couplings between a secondary dark boson and the SM photon. This operator may arise, e.g., at the one-loop level from a theory connecting fermions charged under $U(1)_{em}$ to additional scalar and vector fields, or from the $\pi^0\gamma X$ vertex in our single-mediator, hadrophillic scenario at the χPT level. This opens a scattering channel similar to axion photoconversion or Primakoff scattering, except instead of the SM photon being in the t channel, the secondary massive boson takes its place. This process $XN \to \gamma N$ (see Fig. 2) may be coherent if the mediator for the scattering couples to nucleons, provided that the momentum transfer scale $q \lesssim 1/R_n$ for a nuclear size R_n and that the sum of the neutron and proton charges coupled to the mediator is not small, so that the total amplitude picks up a coherent enhancement $\propto (\sum_p Q_p + \sum_n Q_n)^2$. For simplicity we will assume that this coherent enhancement goes according to the proton number squared, Z^2, although depending on the baryonic couplings it could be larger or smaller (for instance, in the case of negative couplings).

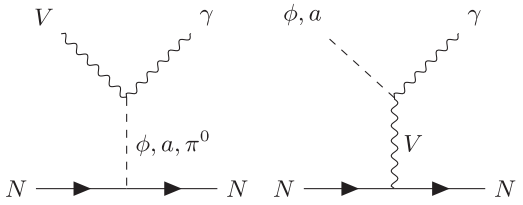

FIG. 2. Left: vector photoconversion via a massive scalar or pseudoscalar mediator. Right: scalar or pseudoscalar photoconversion via a massive vector mediator.

In the case of scalar photoconversion on a nucleus of mass M via a heavy vector mediator V, we have

$$\langle|\mathcal{M}|^2\rangle_{\mathrm{V}}^{\phi\to\gamma} = (g_n\lambda^s)^2 t[2M^2(m_\phi^2 - 2s - t) + 2M^4 - 2m_\phi^2(s+t) + m_\phi^4 + 2s^2 + 2st + t^2] \times \frac{F_N^2(t)}{(8(m_V^2 - t)^2)}, \quad (9)$$

where s, t are the Mandelstam invariants for the center of momentum energy and momentum transfer, respectively. The nuclear form factor $F_N^2(t)$, for which we take the well-known Helm parametrization with normalization $F_N^2(0) = Z^2$. The same matrix element holds in the case of pseudoscalar photoconversion $a \to \gamma$. For vector photoconversion via a heavy scalar or pseudoscalar mediator, the spin-averaged matrix elements are

$$\langle|\mathcal{M}|^2\rangle_{\mathrm{S}}^{V\to\gamma} = \frac{3(g_n^s\lambda^s)^2(4M^2 - t)(m_V^2 - t)^2}{16(m_\phi^2 - t)^2}F_N^2(t) \quad (10)$$

$$\langle|\mathcal{M}|^2\rangle_{\mathrm{P}}^{V\to\gamma} = \frac{(g_n^p\lambda^p)^2(-t)(m_V^2 - t)^2}{8(m_a^2 - t)^2}F_N^2(t). \quad (11)$$

For each case we check that the free matrix element is peaked in the momentum transfer, t, well within the coherent regime of momentum transfers where the Helm form factor is flat and unsuppressed. We find that the matrix element only starts to leave the coherent regime for large incoming energies $E_X \gtrsim 500$ MeV and for heavy mediator masses $m_Y \gtrsim 300$ MeV. Above this energy scale and above this heavy mediator limit, there may be a growing inelastic/incoherent component, but to avoid theoretical complications in this crossover regime between coherence and incoherence, we primarily consider the $m_Y \lesssim 300$ MeV regime.

The cross sections associated with these matrix elements are shown in Fig. 3. Notice that since in the case of an incoming vector photoconverting via a heavy scalar or

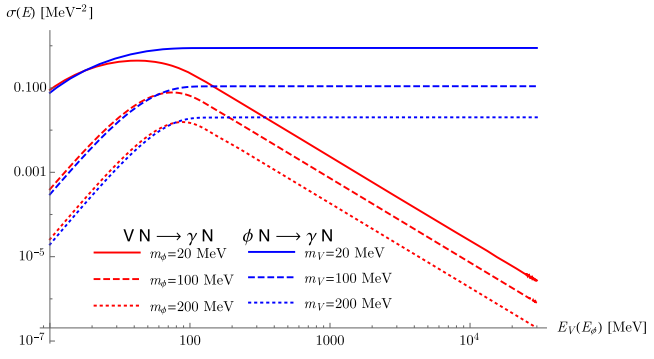

FIG. 3. Cross sections for the photoconversion of a massive vector (scalar) mediated by a massive scalar (vector) through the dimension-5 vertex. We fix the mass of the incoming boson to 1 MeV in each case. The cross sections in the case of the photoconversion of a massive pseudoscalar are similar, varying only up to a constant factor.

pseudoscalar, $\langle|\mathcal{M}|^2\rangle_{\mathrm{S,P}}^{V\to\gamma}$ has no s dependence, and therefore the total cross section picks up its s dependence only as $\sim 1/s^2$ from the Lorentz invariant phase space integration. The phenomenological impact of this difference between (pseudo)scalar-mediated and vector-mediated photoconversion is seen in Fig. 3 as either a decreasing or constant cross section as a function of the energy of the incoming boson, thereby impacting the fit at MiniBooNE in the high-energy/low-energy bins.

Finally, let us discuss the last possibility which arises from the effective dimension-5 coupling of a massive vector to the pion anomalous decay; $\mathcal{L} \supset \pi^0 F_{\mu\nu}\tilde{H}^{\mu\nu}$. This effective interaction vertex typically appears in any $U(1)_X$ model where V interacts with the SM quarks, resulting in a $\pi^0 - \gamma - V$ vertex at the pion level. Models involving this interaction vertex that satisfy the MiniBooNE excess are discussed in Ref. [44]. This interaction permits $VN \to \gamma N$ via the pion-nucleon interaction $ig_{\pi NN}\pi^0\bar{\psi}\gamma^5\psi$, where the πNN coupling is estimated around $g_{\pi NN} \simeq 13$ [55].

Given that the neutral pion coupling $g_{\pi NN}\bar{N}\gamma^5\tau_3 N\pi^0$ is opposite in sign for the proton and neutron, which have opposing isospin charges, $VN \to \gamma N$ scattering via coherent π^0 exchange is suppressed for most isotopes $[\propto(A-2Z)^2]$. Instead, we consider single-nucleon scattering such that the process is incoherent and proportional to $AF_p^2(t)$, where $F_p(t)$ is the proton form factor, and we take $M = m_p, m_n$.

In the absence of a full nuclear model, we approximate this scattering on free nucleon initial and final states. Since we are primarily concerned with the electromagnetic component of the signal to explain the MiniBooNE anomaly, here we only take the final state photon as the visible energy and do not treat the physics of the nucleon final state. For the low energy excess, we find that most of the final state energy is carried by the photon. However, this nucleon final state may be relevant for studies in liquid argon time projection chambers (LArTPCs) that can identify the tracks of ejected nucleons, so we leave this to a future study. Additionally, whether the final state nucleon is ejected or not, it may be likely that the nucleus is left in an excited state. The deexcitation photons released from nuclear transitions may also contribute to the signal, but with only $\mathcal{O}(1\ \mathrm{MeV})$ of energy. This signal component may not be relevant for experiments with high energy thresholds (e.g., MiniBooNE, MicroBooNE) but could be relevant for liquid scintillators and especially the LSND anomaly. We leave this subject to a future work.

IV. ANALYSIS OF THE MINIBOONE DATA AND CONSTRAINTS

A. MiniBooNE target-mode and beam-dump-mode data

We simulate the LLP flux and event spectra in the MiniBooNE detector by first modeling the flux of charged pions focused by the magnetic horns. This involves a detailed simulation of the Lorentz forces acting on the charged pions and their radiative transport through the horn system, discussed more in Appendix A. Once the charged pion decays are modeled with the decay channels discussed in the previous section, the LLPs produced in these decays are propagated towards the detector and integrated over its geometrical angular acceptance. This is done for forward and reverse horn currents, corresponding to the neutrino and antineutrino mode data, respectively [1–3], and separately for the charged and neutral pion decays in the MiniBooNE beam dump without horn focusing [4]. Since the timing structure of the excess falls within 7 ns relative to the neutrino time of flight, we expect LLP masses above $\simeq 20$ MeV will begin to be less consistent with this timing structure due to their smaller boost factors. We do not employ a hard timing cut in this work, but instead limit our scope to masses below 35 MeV, above which this effect should become prominent. Their subsequent scattering via photoconversion processes $XN \to \gamma N$ gives the distribution of E_{vis} (for which we take equal to E_γ for simplicity, although in principle a smearing matrix should be applied to more diligently model the detector resolution) and $\cos\theta_\gamma$ for the reconstructed Cherenkov rings. Given a set of couplings in the decay and scattering models, and the masses of the LLP and the scattering mediator, we then derive fits to the MiniBooNE data.

Example fits to the ν-mode cosine and visible energy spectra are shown in Fig. 4. In the absence of full two-dimensional data across $(E_{\mathrm{vis}}, \cos\theta)$ and covariance matrices for both neutrino-mode and antineutrino-mode data, we compute a binned χ^2 for both the visible energy data and cosine data for N bins:

$$\chi^2_\nu = \sum_{i=1}^{N} \frac{(d_i - s_i - b_i)^2}{\sigma_i^2}. \tag{12}$$

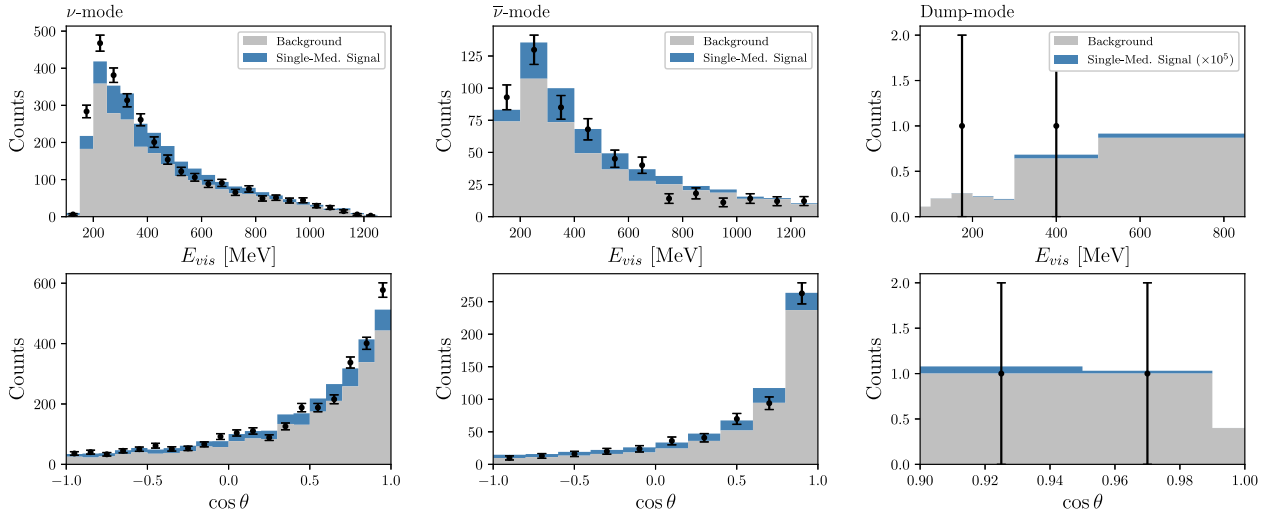

FIG. 4. An example fit to the energy and cosine spectra in the MiniBooNE ν-mode (left), $\bar{\nu}$-mode (center), and beam-dump-mode (right) with a long-lived vector (V) produced from the IB2 decay of the charged pions and scattering into a single-photon final state via the SM π^0-nucleon interaction [see Eq. (17)]. Here the signal in the beam-dump-mode is scaled up by a factor of 10^5 for visualization.

We then pick the more constraining of the two, either from the cosine or the visible energy data, to set the confidence levels. A similar χ^2 is constructed for the antineutrino-mode data and the beam-dump-mode data, and we combine all three datasets together in a joint χ^2:

$$\chi^2_{\mathrm{MB}} = \chi^2_{\nu} + \chi^2_{\bar{\nu}} + \chi^2_{\mathrm{dump}}. \tag{13}$$

In each model, the signal yield will be schematically proportional to branching ratio in the three-body decay times scattering cross section; the yield will scale with the coupling product $g^2\lambda^2 y^2$. For the operator combinations in model A, we generally fix the mass of the long-lived boson and allow the coupling product and the mass of the mediator in the photoconversion scattering to float in the fit.

It is important to note that the MiniBooNE excess is in time with the booster neutrino beamline 52 MHz beam timing structure [3], strongly suggesting that the source of the excess is relativistic. This is to be expected from neutrinos or other light particle propagation (studied in this paper) from the target to the detector.

B. MicroBooNE $1\gamma 0p$ data

The MicroBooNE collaboration performed an analysis of $\Delta \to N\gamma$ resonant production utilizing several final state topologies, namely $1\gamma 0p$ and $1\gamma 1p$ [62]. We calculate the expected event rate at MicroBooNE, again employing the simulation procedure for the charged and neutral pions produced in the BNB target and focused through the horn system working in neutrino-mode polarization. This procedure follows exactly as in the previous section for the MiniBooNE analysis, as described in Appendix A, except we now integrate the pion decay products over the solid angle spanned by the MicroBooNE detector's geometric cross section. In Fig. 5 we show example event spectra produced from three-body charged meson decays as well as from two-body π^0 decays using the VIB2 interaction model with couplings to the pion doublet.

One could also investigate the possibility of using the existing data of higher-energy beam dump experiments like CHARM (400 GeV) or MINERνA (120 GeV) to constrain the model parameter space. In the case of CHARM, we estimate $\mathcal{O}(10^{17})$ pions produced for 2×10^{18} collected protons on target (POT) [63], and for a detector proximity of 480 meters, the expected flux of LLPs above the 5 GeV energy threshold should be comparatively smaller

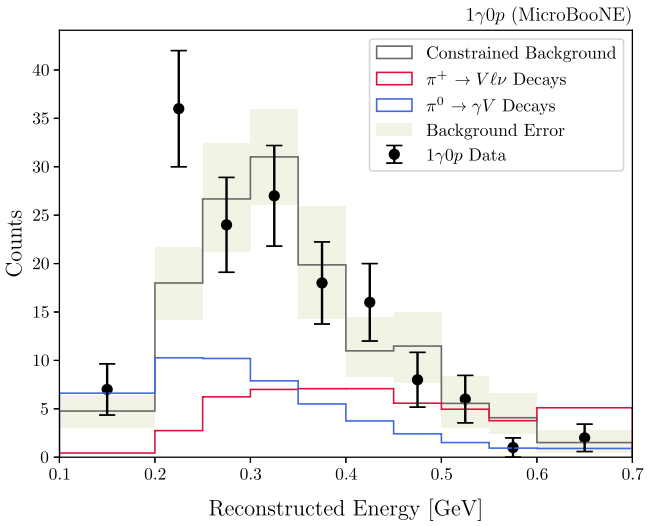

FIG. 5. Example event spectra prediction from two-body decays of $\pi^0 \to \gamma V$ (blue) and three-body decays of $\pi^+ \to \ell\nu V$ (red) at MicroBooNE in the $1\gamma 0$p topology. Here the LLP mass m_V is fixed to 5 MeV.

than those from LSND and KARMEN. Similarly, for MINERνA, one might examine the $\nu - e$ elastic scattering cross section measurements for events that would mimic the 1γ final state considered in our phenomenological models [64]. Although the beam energy at MINERνA is larger (NuMI beam) than the BNB flux at MicroBooNE, the detector tonnage at the latter is bigger given comparable collected POT and detector baselines. Hence, we limit the scope of this analysis to deriving the more stringent constraints from the null results of the MicroBooNE data.

C. Constraints from the LSND and KARMEN null results

The parameter space associated with these scenarios gets constrained by the LSND data. The LSND experiment used a 800-MeV proton beam. Three analyses, $e^- - \nu_e$ elastic scattering [65], charged current reactions of ν_e on ^{12}C [66], and neutrinos from the pion decay in flight [67], can be used to obtain constraints for the parameter space relevant to this solution to the MiniBooNE excess. The data from the elastic and inelastic analyses provide a constraint for the electromagnetic energy in the range 18–35 MeV while the decay-in-flight analysis provides a constraint for the energy range 60–200 MeV.

A summary of the efficiencies and observed counts in each channel is given in Table I. To determine the constraints set by the null results of each channel on the parameter space of the decay and scattering models we consider, we adopt a single-bin χ^2 as a crude test statistic. For example, using the decay-at-rest (DAR) analysis, we look for a contour of constant $\Delta\chi^2 = s^2/1081$, where s is the expected $XN \to \gamma N$ events (multiplied by a flat 37% efficiency) in the energy range [18, 35] MeV and 1081 is the number of observed events in the DAR region of interest. Finally, it may be important to additionally consider inelastic responses of the nucleus in $XN \to \gamma N$ scattering. Although the scope of this work is limited to the null results of LSND, one might also attempt to explain the LSND excess via the inelastic scattering of $XN \to \gamma N^*$, $N^* \to N\gamma$, which, as mentioned in Sec. III, would show up as gamma signal from nuclear deexcitation but will be left to a future work.

Next, we can apply the KARMEN experiment's observations of the neutral current excitation process $^{12}\mathrm{C}(\nu,\nu') \to {}^{12}\mathrm{C}(1^+, 1; 15.1\ \mathrm{MeV}\gamma)$ to place a constraint on photon final states arising from the photoconversion scattering in our phenomenological models [68]. This data consists of 4.6×10^{22} collected POT on the tungsten target at the ISIS [69,70]. The KARMEN detector was situated 17.5m from the target and totaled 56t of liquid scintillating hydrocarbon in a 3.5 m × 4 m × 4 m geometry. To recast the NC analysis in Ref. [68] for our signal model, we will assume the same 12% signal efficiency and 11.5% energy resolution.

TABLE I. Kinematic regions of interest in the LSND decay-at-rest (DAR) and decay-in-flight (DIF) analyses, their signal efficiencies, and the target number of statistically significant signal counts.

Analysis	E_{vis} range	$\cos\theta$ range	Efficiency	Counts
DAR	[18, 35] MeV	$-1 \le \cos\theta \le 1$	37%	1081
DIF	[60, 200] MeV	$\cos\theta < 0.8$	10%	50

V. ANALYSIS OF THE CCM120 DATA AND CCM200 PROJECTIONS

In 2019 a six week engineering beam run was performed with the CCM120 detector, named due to it having 120 inward pointing main photomultiplier tubes (PMTs). The CCM120 experiment met expectations and performed a sensitive search for sub-GeV dark matter via coherent nuclear scattering with 1.79×10^{21} protons on target (POT) [71,72]. Because of the intense scintillation light production and short 14 cm radiation length in LAr [73], the relatively large CCM detector has good response to electromagnetic signal events in the energy range from 100 keV up to hundreds of MeV.

Another key feature of CCM is that it uses fast beam and detector timing to isolate prompt ultrarelativistic particles originating in the target. This can distinguish signal from the significantly slower neutron backgrounds that arrive approximately 225 ns after the start of the beam pulse (relativistic particles traverse the 23 m distance in 76.6 ns) [71]. Furthermore, the Lujan beam low duty factor of $\sim 10^{-5}$ and extensive shielding are efficient at rejecting steady state backgrounds from cosmic rays, neutron activation, and internal radioactivity from PMTs and ^{39}Ar.

In order to determine the sensitivity reach of CCM's ongoing run, we use the beam-on background distribution determined from the recent CCM120 run [71], with a further expected factor of 100 reduction from extensive improvements in shielding, veto rejection, energy and spatial resolution, particle identification analysis, and reduced beam width. Further details of the signal gamma-ray and electron event reconstruction and background rejection analysis are detailed in the recent CCM120 ALP search [51], which shares many similarities.

Since our MiniBooNE excess explanation requires dominant contributions from the charged pion decay (otherwise the data in the beam-dump mode measurement would rule it out), the constraint for this parameter space mostly emerges from the elastic and inelastic analyses. The visible energy distribution for the events at CCM120 is in the range 10–70 MeV (as shown in Fig. 6) for various scenarios described in Sec. II. In Fig. 7, we show the allowed parameter space where the MiniBooNE excess can be explained after satisfying the LSND constraints, in addition to the comparison with projected sensitivities for CCM assuming the null hypothesis.

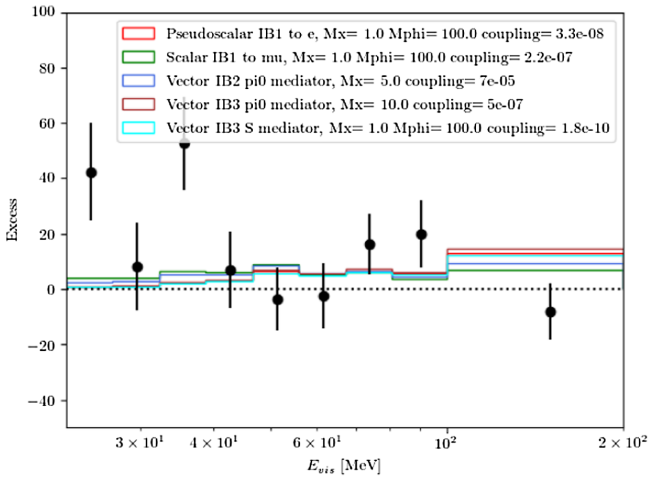

FIG. 6. The CCM120 high energy subtraction spectrum used for the search. Only events between 22.4 and 200 MeV reconstructed energy were included in this spectrum. Also shown are example spectra from the dark sector for the five models tested with CCM120, using points on the 68% confidence level.

VI. RESULTS

In Fig. 7 we show the resulting constraints set by the CCM120 data, projections for CCM200 along with the preferred MiniBooNE regions (C.L.s at 1σ and 2σ), and the constraints from the LSND DIF and DAR analyses (see Table I) for three possible decay models and scattering model scenarios. These models are named according to (i) the type of long-lived boson and decay mode (see Fig. 1), e.g., scalar IB1μ to indicate the IB1 decay channel through a coupling to the muon leg, and (ii) the type of mediator (scalar, pseudoscalar, or vector) used in the scattering via the interactions in Fig. 2. All curves correspond to 95% C.L. Also shown are the limits extracted from the MicroBooNE $1\gamma 0p$ data.

Beginning with Fig. 7 (left), we consider the parameter space for a long-lived scalar particle ϕ produced via the IB1 decay $\pi^{\pm} \to \mu\nu\phi$ through a muonic coupling, and scattering through $\phi N \to \gamma N$ photoconversion via a massive vector mediator V (see also Secs. II and III for details). The decay and scattering are described by the phenomenological Lagrangian,

$$\mathcal{L}_{\text{int}} \supset g_{\mu}^{S}\phi\bar{\mu}\mu + y_{n}^{V}V_{\mu}\bar{N}\gamma^{\mu}N - \frac{\lambda_S}{4}\phi F_{\mu\nu}H^{\mu\nu} + \text{H.c.}, \tag{14}$$

with $H_{\mu\nu} \equiv \partial_{\mu}V_{\nu} - \partial_{\nu}V_{\mu}$ and vector mass $m_V > m_{\phi}$. The event rate is proportional to the coupling product $g_{\mu}^{S}y_{n}^{V}\lambda_S$. For this setup, we can fix the mass of the long-lived scalar to 20 MeV and vary m_V, for which we find that the fit to the MiniBooNE target and dump mode data lies around the scale $g_{\mu}^{S}y_{n}^{V}\lambda_S \simeq 10^{-9}$ MeV^{-1} at the 1σ and 2σ levels. The black hatched region is constrained by the CCM120 data, while constraints by LSND shown in olive are more stringent but do not rule out any of the preferred parameter space from the MiniBooNE fit—conversely, MicroBooNE's $1\gamma 0p$ data excludes more parameter space up to about a factor of 2 larger in the coupling product across all mediator masses, and one could expect that future SBN experiments with larger detector exposure could test the MiniBooNE preferred region completely.

In Fig. 7 (center), the parameter space for a long-lived pseudoscalar coupling to electrons and produced through IB1 $\pi^{\pm} \to e\nu a$ decays is shown as a function of the coupling product and mass of a vector mediator taking place in the $aN \to \gamma N$ scattering via similar interactions,

$$\mathcal{L}_{\text{int}} \supset -ig_{e}^{P}a\bar{\mu}\gamma^{5}\mu + y_{n}^{V}V_{\mu}\bar{N}\gamma^{\mu}N - \frac{\lambda_P}{4}aF_{\mu\nu}\tilde{H}^{\mu\nu} + \text{H.c.} \tag{15}$$

We fix the pseudoscalar mass $m_a < 2m_e \simeq 1$ MeV, otherwise $a \to e^{+}e^{-}$ decays would be kinematically allowed and may be incompatible with the excess signal, and again take $m_V > m_a$. In this scenario the event rate is proportional to the coupling product $g_{e}^{P}y_{n}^{V}\lambda_P$, and a result similar to

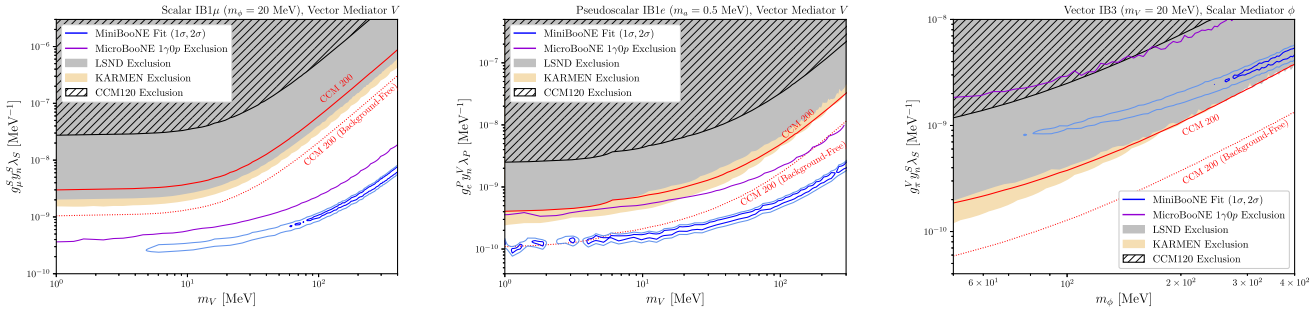

FIG. 7. Parameter space for the two-mediator models, consisting of one long-lived boson produced through charged pion three-body decays and scattering via a secondary heavy mediator are shown. Left: a 20 MeV scalar ϕ coupling to muons and scattering via a vector mediator V as in Eq. (14). Center: a 0.5 MeV pseudoscalar a coupling to electrons and scattering via a vector mediator V as in Eq. (15). Right: a 20 MeV vector V coupling through the IB3 pion contact interaction and scattering via a massive scalar ϕ as in Eq. (16). The exclusions (CCM120, KARMEN, LSND, and MicroBooNE) and projections for CCM200 are shown at 95% C.L., while the MiniBooNE fits are shown at 68% and 95% C.L. in dark and light blue, respectively.

Fig. 7 (left) is found where the entirety of the MiniBooNE preferred region is allowed by the existing constraints we have considered.

In Fig. 7 (right) we consider a third scenario in which a massive vector mediator is long-lived and couples to the charged pion through contact interactions, and subsequently scatters via a massive scalar mediator with mass $m_\phi > m_V$. We take the effective interaction Lagrangian,

$$\mathcal{L}_{\rm int} \supset y_n^S \phi \bar{N} N - \frac{\lambda_S}{4} a F_{\mu\nu} \tilde{H}^{\mu\nu} - i g_\pi^V \pi^+ \bar{\mu} \gamma^\rho (1-\gamma^5) \nu V_\rho + \text{H.c.} \tag{16}$$

However, in this case we find that the favored parameter space to explain the MiniBooNE excess is largely ruled out at 95% C.L. by LSND and KARMEN.

In the second class of phenomenological model, we consider a single long-lived vector mediator that couples to quarks and enters the pion sector via the χ-PT Lagrangian in Eq. (17):

$$\mathcal{L}_{\rm int} \supset i g_{\pi^\pm} V_\mu \pi^+ (\partial^\mu \pi^-) + g_{\pi^0} \frac{e}{16\pi f_\pi} \pi^0 F_{\mu\nu} \tilde{H}^{\mu\nu} - i g_{\pi NN} \pi^0 \bar{N} \gamma^5 \tau_3 N. \tag{17}$$

See again Secs. II and III for more details. In Fig. 8 we show the parameter space sensitivities and constraints for the IB2 decay model for $m_V = 5$, 10, 20 MeV. The C.L.s for the MiniBooNE fit are shown (blue) for the combination of ν, $\bar{\nu}$, and beam-dump-mode runs, exclusions set by the CCM120 engineering run are shown by the black hatched region, and future sensitivity expected in CCM200 with upgrades (red). Also shown are constraints from LSND (light yellow), KARMEN (brown), and rare charged pion decay searches from PIENU (gray). In this case we have production channels from both charged pion decays ($\pi^\pm \to \ell \nu V$), for which we take the IB2 decay mode as a benchmark, and neutral pion decays ($\pi^0 \to V\gamma$). Constraints from $\pi^\pm$ decay width measurements can be directly applied to this parameter space in terms of $g_{\pi^\pm}$, and for these we take the bounds from PIENU [74] which have set constraints on invisible radiative decays $\pi^\pm \to e^\pm \nu X$ and $\pi^\pm \to \mu \nu^\pm X$ dependent on the X mass.

Since the neutral pion decay channel is active in this scenario, it can dominate as a production channel to produce the LLP at the lower-energy beam target experiments (CCM, LSND, and KARMEN) where both the charged and neutral pions are isotropic. This contrasts with the case of MiniBooNE and MicroBooNE that take advantage of the magnetic focusing horns to enhance the fluxes driven from the charged pion decays. This results in a few qualitative differences, namely that at the lower-energy beam targets, the neutral pion decays will produce relatively more energetic LLPs than the charged pions (contrast this with the case in Fig. 5, for example). These neutral pion decay energies can be up to $\mathcal{O}(100)$ MeV, where the cross section of scattering is also larger (see Fig. 3). These factors suppress the event rates at KARMEN, whose energy region of interest is limited below 40 MeV; hence, we see a more stringent exclusion from CCM120 relative to KARMEN in Fig. 8 in spite of KARMEN having more exposure and a larger detector size. On the other hand, LSND does set a more stringent exclusion, but it is also limited in reach due to the detector being only 12 degrees off axis, capturing only the tail of the neutral pion momentum distribution which peaks instead at 90 degrees off axis.

In Fig. 8 we also observe an interesting trend as a function of the vector mass. As the vector mass transitions from 5 to 35 MeV, the preferred solution transitions from one in which the signal is dominated by the charged pion decay channel to one where both charged and neutral meson decays are contributing to the signal in MiniBooNE equally. In this limiting case at $m_V = 35$ MeV, the

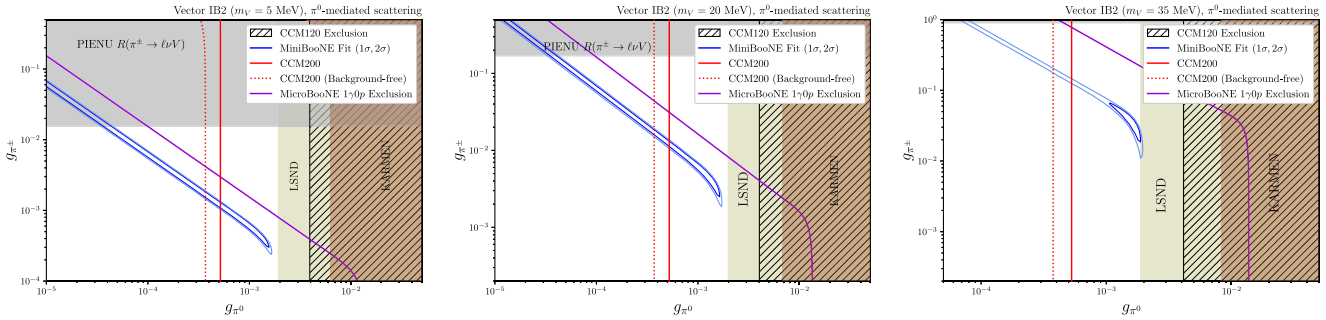

FIG. 8. Parameter space for the single mediator scenario where a massive vector V couples to the pion doublet via charged pion coupling $g_{\pi^\pm}$ and neutral pion coupling g_{π^0} as in Eq. (17). The production channels via these couplings are therefore neutral pion decay $\pi^0 \to \gamma V$ and IB2 decay $\pi^\pm \to \ell \nu V$, while the detection takes place via π^0-mediated $VN \to \gamma N$ scattering. We vary the vector mass m_V from left to right as 5 MeV (left), 10 MeV (middle), and 35 MeV (right). The exclusions (CCM120, KARMEN, LSND, and MicroBooNE) and projections for CCM200 are shown at 95% C.L., while the MiniBooNE fits are shown at 68% and 95% C.L. in dark and light blue, respectively.

preferred couplings to explain the MiniBooNE excess lie in the closed contour where $g_{\pi^\pm} \simeq g_{\pi^0}$, as shown in the right plot of Fig. 8. This range of parameter space is not yet excluded by LSND at the 95% C.L. In addition, constraints from π^0 decay width measurements apply to the g_{π^0} coupling in this parameter space, but they apply only to larger values of the coupling that are not shown in the plot. The constraints from PIENU also begin to relax while moving to larger masses, due to the weaker branching ratio of $\pi^+ \pm \to \ell \nu V$ with higher mass (see, e.g., Fig. 14).

While we have only shown three mass points here, these trends are expected to hold through to the kinematic upper limit of the kinematically allowed vector boson mass in the two-body and three-body decays, $m_V \lesssim m_\pi$. For lower masses, the landscape of constraints relative to the MiniBooNE fit will be very similar to the case in Fig. 8, left, except globally shifted to lower $g_{\pi^\pm}$ couplings to compensate for the larger branching ratios at lower masses. The relevant constraint that should apply at lower masses would be from cosmological considerations; we generically expect a limit on the mass $m_V \lesssim 10$ MeV due to its impact on $\Delta N_{\rm eff}$ [75], which is, however, model dependent.

VII. CONCLUSIONS

The rare three-body decays of charged pions and kaons to new states in the MeV mass scale as a dark-sector explanation for the MiniBooNE excess has shed light on a potential correlation between the mesonic sector and new physics solutions. By investigating an extended range of phenomenological models, we have demonstrated that these scenarios, incorporating long-lived particles generated in the three-body decays of charged mesons and two-body anomalous decays of neutral mesons, can be consistent with constraints from LSND, KARMEN, and MicroBooNE experiments. In particular, we found that in the context of these models with a long-lived particle and a heavy mediator to facilitate photoconversion scattering, the MiniBooNE excess data preferred a mediator in the mass range $m_Y \gtrsim 10$–100 MeV. In all cases, scattering with detector atomic nuclei was considered, so it may be interesting to probe new mediators in this mass range with generalized hadronic couplings in separate experiments. Second, the inelastic nuclear responses to the mediators we have considered are an interesting possibility to study, namely in the context of the LSND excess which we have set aside for the time being. One could also examine the same inelastic channels as they contribute to the event spectra at KARMEN, MiniBooNE, MicroBooNE, and CCM, although this requires a detailed shell-model description of the nucleus coupled to the new mediators we have used.

The forthcoming analysis of the current CCM200 data taking campaign will have the ability to test dark-sector explanations to the MiniBooNE excess, especially for new long-lived particles coupled to the pion doublet; as a stopped-pion experiment, it can leverage the neutral pion production and its close proximity to the proton beam target. In this way, stopped-pion experiments have more sensitivity via the neutral pion channels to probe this set of solutions in a complementary way to short baseline experiments, whose magnetic horns produce instead a focused flux of charged mesons. Long-lived vector mediators that couple to the pion doublet around 5 MeV in mass, as preferred by the fits to MiniBooNE data, are now susceptible to searches through both stopped-pion experiments as well as rare meson decay searches. Though not within the scope of this work, there is no reason to not expand the dark sector couplings to the meson octet which would include kaons, or to the broader hadronic spectrum of baryons and vector mesons. This analysis motivates such cases through the advantage of correlated couplings which open up multiple production and detection channels to constrain, and hopefully discover, solutions to anomalies in this fashion.

ACKNOWLEDGMENTS

We thank Michael Shaevitz and William Seligman for the dedicated programming work and feedback on the modelB routines for particle transport in the BNB horn system. We also thank Wooyoung Jang for the simulation work on the MiniBooNE pion fluxes and Noemi Rocco for the useful discussions. A. A. A.-A., J. C. D., and M. C.-E. acknowledge support from DGAPA-UNAM Grant No. PAPIIT-IN104723. We acknowledge the support of the Department of Energy Office of Science, Los Alamos National Laboratory LDRD funding, and funding from the National Laboratories Office at Texas A&M. We acknowledge that portions of this research were conducted with the advanced computing resources provided by Texas A&M High Performance Research Computing. We also wish to acknowledge support from the LANSCE Lujan Center and LANL's Accelerator Operations and Technology (AOT) division. This research used resources provided by the Los Alamos National Laboratory Institutional Computing Program, which is supported by the U.S. Department of Energy National Nuclear Security Administration under Contract No. 89233218CNA000001.

APPENDIX A: MESON FLUX SIMULATIONS AT THE BNB

To simulate the focused charged meson decays that take place in the BNB horn system, we begin by simulating the proton beam spot that sources the charged mesons, shown in Fig. 9, based on the normal distribution of protons given in [76] which source a $\pi^\pm$ at beam spot position (x, y) and depth z into the target given from the interaction probability $1 - e^{-\sigma(p) n z}$ based on the pion production cross section in Eq. (A2) and Be density $n = 1.85$ g/cm^3. The proton momenta are also generated by a parametrization. We use this beam spot to generate a Monte Carlo sample of pion production vertices. Their momenta and production angles

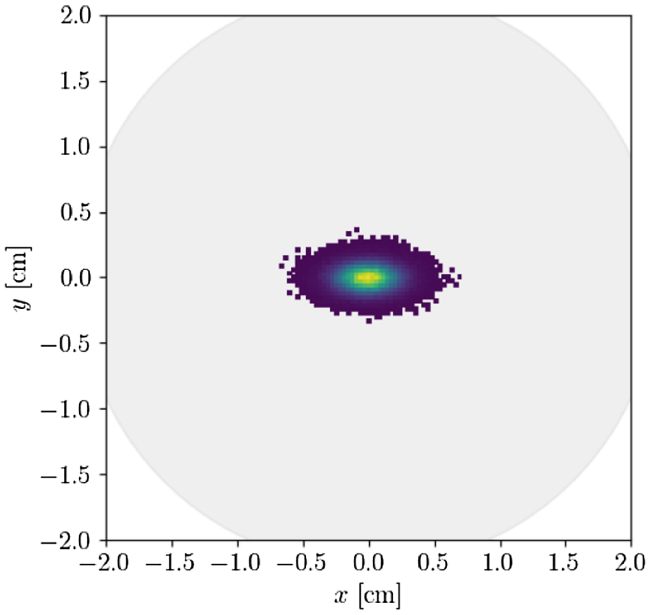

FIG. 9. Simulation of the BNB beam spot distribution of protons on target as a function of (x, y) over the face of the Be target, shown in gray.

with respect to the progenitor proton direction can be expressed using the Sanford-Wang parametrization given in Ref. [77], shown in Fig. 10. This scheme parametrizes the total pion production cross section as follows;

$$\frac{\partial^2\sigma(p+\mathrm{Be}\to\pi^\pm+X)}{\partial p\partial\Omega} = c_1 p^{c_2}\left(1-\frac{p}{p_B-c_9}\right) \times \exp\left(-c_3\frac{p^{c_4}}{p_B^{c_5}}-c_6\theta(p-c_7 p_B(\cos\theta)^{c_8}\right), \quad \text{(A1)}$$

TABLE II. Sanford-Wang cross section parameters at the BNB target.

Type	c_1	c_2	c_3	c_4	c_5	c_6	c_7	c_8	c_9
π^+	220.7	1.080	1.0	1.978	1.32	5.572	0.0868	9.686	1.0
π^-	213.7	0.9379	5.454	1.210	1.284	4.781	0.07338	8.329	1.0

where the constants associated with π^+ (π^-) production are repeated in Table II for convenience, while the total cross section is parametrized as

$$\sigma(p) = a + bp^n + c(\ln(p))^2 + d\ln(p) \quad \text{(A2)}$$

with

$$a = 307.8$$
$$b = 0.897$$
$$c = -2.598$$
$$d = -4.973$$
$$n = 0.003. \quad \text{(A3)}$$

Taking the position (x, y, z) from the beam spot simulation and the momentum, polar angle, and azimuthal angle $(p, \cos\theta, \phi)$ from a weighted MC simulation of the Sanford-Wang cross section, the pion flux is prepared for simulated transport through the remainder of the beam target and horn system. For this we use a simple geometric model of the BNB horn shape and magnetic field profile as inputs to a Runge-Kutta charged particle transport routine. Some sample trajectories are shown in Fig. 11.

The post-horn flux distribution using 5×10^5 simulated POT is shown in Fig. 12 as a function of pion angle with respect to the beam axis. For comparison, the equivalent detector solid angle coverages of MicroBooNE and

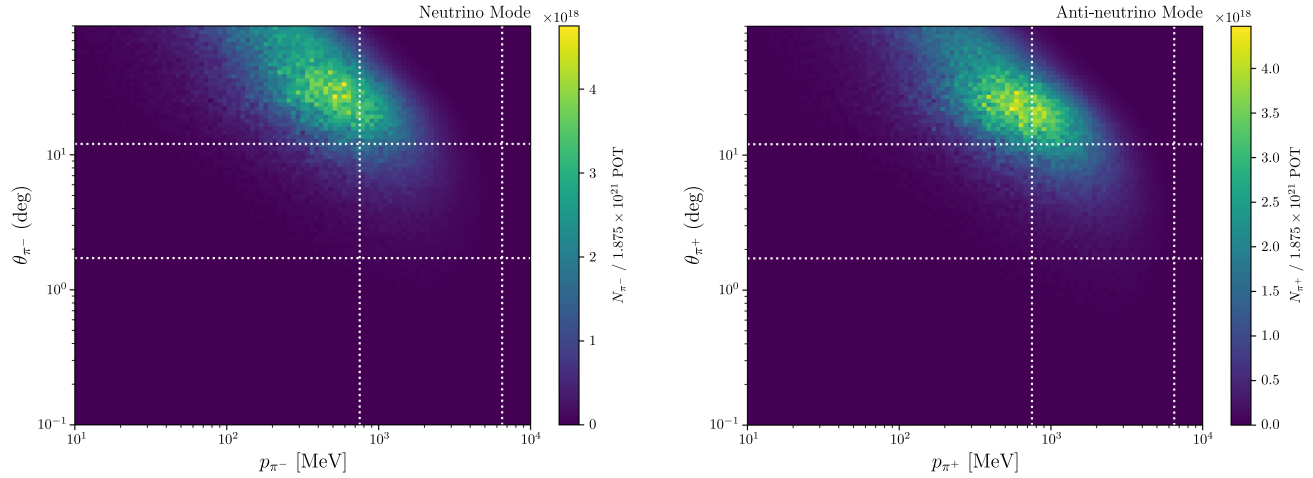

FIG. 10. Charged pion fluxes produced at the BNB via a Monte Carlo treatment of the Sanford-Wang parametrization of the charged pion production cross section.

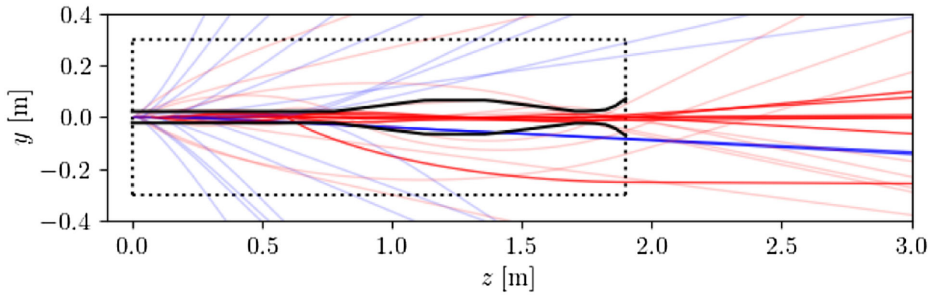

FIG. 11. Simulation of the BNB horn with example trajectories showing the π^+ (red) and π^- (blue) transport in the horn system for the forward horn current (FHC) polarization.

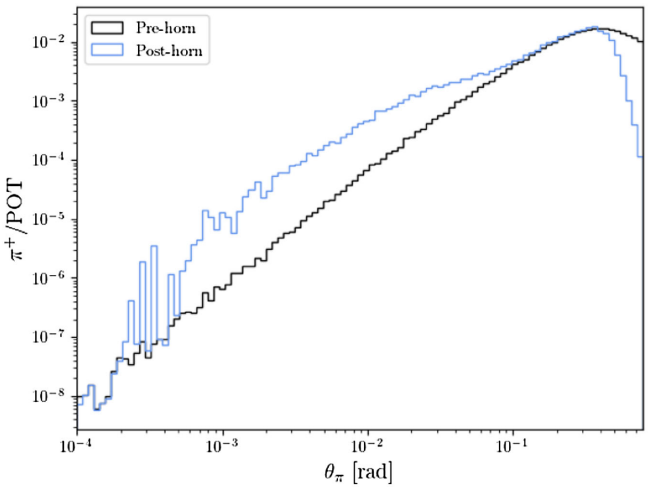

FIG. 12. The prehorn π^+ flux (black) using the Sanford-Wang parametrized cross section convolved with the BNB proton beamspot, and the posthorn flux (blue) after modeling the transport through the magnetic horn system are both shown as a function of the pion angle with respect to the beam axis. In both cases 5×10^5 simulated POT were used.

MiniBooNE are 1.2 and 3 mrad, respectively. We validate this distribution in a pragmatic way by checking that it predicts a neutrino spectrum at the MiniBooNE detector that is consistent with what is reported by the collaboration. To do this, we take the focused $\pi^\pm$ fluxes predicted by Sanford-Wang and perform a two-body decay Monte Carlo algorithm on the charged pions, allowing them to decay to ν_μ, μ at some distance x away from the production site in the target, where x itself is drawn from a distribution like $\exp(-x/v\tau_{\pi^\pm})$ using the pion lifetimes.

Additionally, the distributions for neutral π^0 that are produced in the BNB target and the dump are shown in Fig. 13. The differences in the π^0 energy and angle distributions at the target versus the dump can be attributed to the larger size of the dump and the differences in material on which the beam impinges. To simulate events from the two-body decays of $\pi^0 \to \gamma X$, we perform the decay simulation in the pion rest frame and boost X into the lab frame. Since X is long-lived and weakly coupled, it can be invisibly transported to the detector. Simultaneously we again check that the X production angle with respect to the beamline is within the detector solid angle.

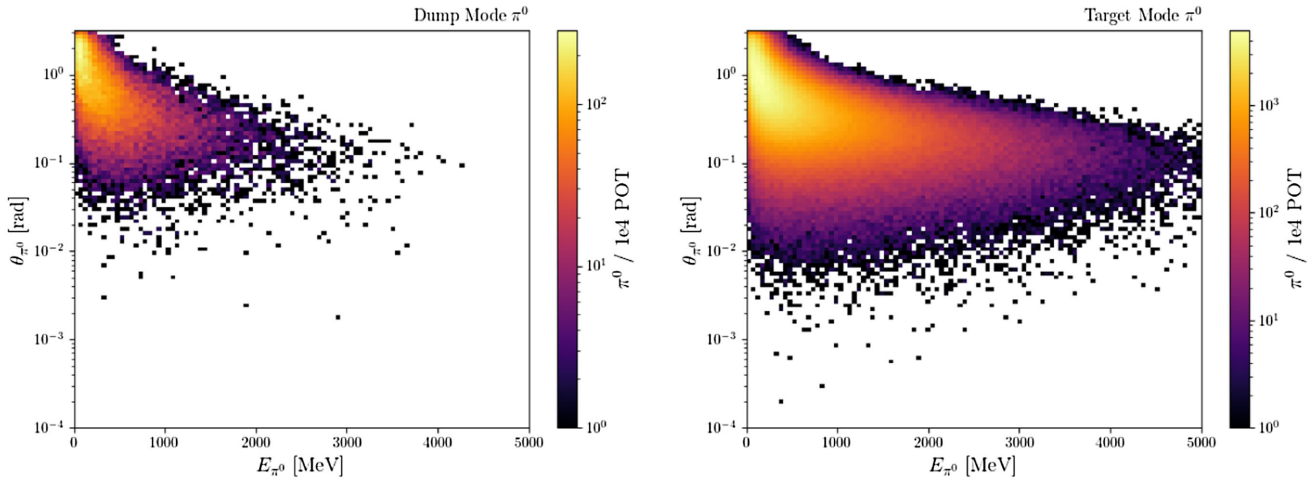

FIG. 13. Beam-dump-mode and target-mode π^0 fluxes, generated from GEANT4 simulation, at the MiniBooNE dump (left) and BNB target (right) as a function of their kinetic energy and angle of travel with respect to the beam axis.

The π^0 kinematic distributions at the MiniBooNE dump and target are shown in Fig. 13, generated from GEANT4 simulation. In each case the rates on the color bar are normalized to 10^4 simulated POT. The discrepancy between the two fluxes, which are $\sim\mathcal{O}(10)$ larger in rate and more energetic in the target mode, can be explained by the choice of material; the target material (Be) has a much lighter nucleus than the dump (steel). Neutral pions produced from protons impinging on the nuclei are long-lived on nuclear scales—$\tau c \simeq 25$ nm for boosted pions—and will undergo multiple scattering and absorption much more often in a heavy nucleus than a light one.

APPENDIX B: TREATMENT OF THREE-BODY DECAY KINEMATICS

For the charged meson three-body decay $M(P) \to \ell(p_1)\nu(p_2)a(p_3)$, we make use of the Dalitz variables $m_{ij}^2 = (p_i + p_j)^2$. In the lab frame, we have

$$m_{12}^2 = (p_1+p_2)^2 = (P-p_3)^2 = M^2 - 2ME_a + m_a^2 \tag{B1}$$

$$m_{23}^2 = (p_2+p_3)^2 = (P-p_1)^2 = M^2 - 2ME_\ell + m_\ell^2 \tag{B2}$$

$$m_{13}^2 = (p_1+p_3)^2 = (P-p_2)^2 = M^2 - 2ME_\nu \tag{B3}$$

$$m_{13}^2 = M^2 + m_\ell^2 + m_a^2 - m_{12}^2 - m_{23}^2. \tag{B4}$$

This set of variables allows us to write

$$d\Gamma = \frac{1}{(2\pi)^3 32M^3}\langle|M|^2\rangle dm_{23}^2 dm_{12}^2 \tag{B5}$$

and reexpress m_{12}^2 in terms of E_a, since $|dm_{12}^2| = 2MdE_a$, allowing us to integrate over m_{23}^2;

$$\frac{d\Gamma}{dE_a} = \int_{(m_{23}^2)_{\min}}^{(m_{23}^2)_{\max}} \frac{1}{(2\pi)^3 16M^2}\langle|M|^2\rangle dm_{23}^2. \tag{B6}$$

This has bounds

$$(m_{23}^2)_{\min}^{\max} = (E_2^* + E_3^*)^2 - \left(E_2^* \mp \sqrt{E_3^{*2} - m_a^2}\right) \tag{B7}$$

with the starred energies defined as

$$E_2^* = \frac{m_{12}^2 - m_\ell^2}{2m_{12}} \tag{B8}$$

$$E_3^* = \frac{M^2 - m_{12}^2 - m_a^2}{2m_{12}}. \tag{B9}$$

Finally, we can integrate over E_a making use of the fact that $m_\ell^2 < m_{12}^2 < M^2 + m_a^2 - 2Mm_a$ to get the E_a limits;

$$m_a < E_a < \frac{M^2 + m_a^2 - m_\ell^2}{2M}. \tag{B10}$$

Using this integration scheme, we show the total branching ratios for IB1, IB2, and IB3/contact decays, broken down by decay channel ($\ell = e$ or $\ell = \mu$), in Fig. 14.

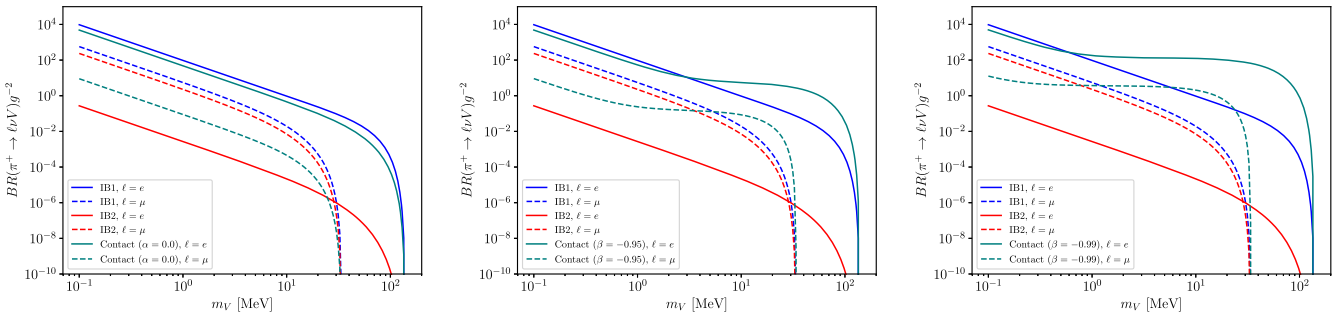

FIG. 14. Branching ratios for vector IB2 and IB3 interactions with various choices of the coefficients of β in Eq. (8) with $\alpha = 1.0$.

[1] A. A. Aguilar-Arevalo *et al.* (MiniBooNE Collaboration), Phys. Rev. Lett. **102**, 101802 (2009).
[2] A. A. Aguilar-Arevalo *et al.* (MiniBooNE Collaboration), Phys. Rev. Lett. **121**, 221801 (2018).
[3] A. A. Aguilar-Arevalo *et al.* (MiniBooNE Collaboration), Phys. Rev. D **103**, 052002 (2021).
[4] A. A. Aguilar-Arevalo *et al.* (MiniBooNE DM Collaboration), Phys. Rev. D **98**, 112004 (2018).

[5] M. Sorel, J. M. Conrad, and M. Shaevitz, Phys. Rev. D **70**, 073004 (2004).
[6] G. Karagiorgi, Z. Djurcic, J. M. Conrad, M. H. Shaevitz, and M. Sorel, Phys. Rev. D **80**, 073001 (2009); **81**, 039902(E) (2010).
[7] G. H. Collin, C. A. Argüelles, J. M. Conrad, and M. H. Shaevitz, Phys. Rev. Lett. **117**, 221801 (2016).
[8] C. Giunti and M. Laveder, Phys. Rev. D **84**, 073008 (2011).
[9] C. Giunti and M. Laveder, Phys. Lett. B **706**, 200 (2011).
[10] S. Gariazzo, C. Giunti, M. Laveder, and Y. F. Li, J. High Energy Phys. 06 (2017) 135.
[11] S. Böser, C. Buck, C. Giunti, J. Lesgourgues, L. Ludhova, S. Mertens, A. Schukraft, and M. Wurm, Prog. Part. Nucl. Phys. **111**, 103736 (2020).
[12] J. Kopp, M. Maltoni, and T. Schwetz, Phys. Rev. Lett. **107**, 091801 (2011).
[13] J. Kopp, P. A. N. Machado, M. Maltoni, and T. Schwetz, J. High Energy Phys. 05 (2013) 050.
[14] M. Dentler, A. Hernández-Cabezudo, J. Kopp, P. A. N. Machado, M. Maltoni, I. Martinez-Soler, and T. Schwetz, J. High Energy Phys. 08 (2018) 010.
[15] K. N. Abazajian *et al.*, arXiv:1204.5379.
[16] J. M. Conrad, C. M. Ignarra, G. Karagiorgi, M. H. Shaevitz, and J. Spitz, Adv. High Energy Phys. **2013**, 163897 (2013).
[17] A. Diaz, C. A. Argüelles, G. H. Collin, J. M. Conrad, and M. H. Shaevitz, Phys. Rep. **884**, 1 (2020).
[18] J. Asaadi, E. Church, R. Guenette, B. J. P. Jones, and A. M. Szelc, Phys. Rev. D **97**, 075021 (2018).
[19] G. Karagiorgi, M. H. Shaevitz, and J. M. Conrad, arXiv:1202.1024.
[20] H. Pas, S. Pakvasa, and T. J. Weiler, Phys. Rev. D **72**, 095017 (2005).
[21] D. Döring, H. Päs, P. Sicking, and T. J. Weiler, Eur. Phys. J. C **80**, 1202 (2020).
[22] V. A. Kostelecky and M. Mewes, Phys. Rev. D **69**, 016005 (2004).
[23] T. Katori, V. A. Kostelecky, and R. Tayloe, Phys. Rev. D **74**, 105009 (2006).
[24] J. S. Diaz and V. A. Kostelecky, Phys. Lett. B **700**, 25 (2011).
[25] J. S. Diaz and A. Kostelecky, Phys. Rev. D **85**, 016013 (2012).
[26] S. N. Gninenko, Phys. Rev. Lett. **103**, 241802 (2009).
[27] S. N. Gninenko and D. S. Gorbunov, Phys. Rev. D **81**, 075013 (2010).
[28] Y. Bai, R. Lu, S. Lu, J. Salvado, and B. A. Stefanek, Phys. Rev. D **93**, 073004 (2016).
[29] Z. Moss, M. H. Moulai, C. A. Argüelles, and J. M. Conrad, Phys. Rev. D **97**, 055017 (2018).
[30] E. Bertuzzo, S. Jana, P. A. N. Machado, and R. Zukanovich Funchal, Phys. Rev. Lett. **121**, 241801 (2018).
[31] P. Ballett, S. Pascoli, and M. Ross-Lonergan, Phys. Rev. D **99**, 071701 (2019).
[32] O. Fischer, A. Hernández-Cabezudo, and T. Schwetz, Phys. Rev. D **101**, 075045 (2020).
[33] M. H. Moulai, C. A. Argüelles, G. H. Collin, J. M. Conrad, A. Diaz, and M. H. Shaevitz, Phys. Rev. D **101**, 055020 (2020).
[34] M. Dentler, I. Esteban, J. Kopp, and P. Machado, Phys. Rev. D **101**, 115013 (2020).
[35] A. de Gouvêa, O. L. G. Peres, S. Prakash, and G. V. Stenico, J. High Energy Phys. 07 (2020) 141.
[36] A. Datta, S. Kamali, and D. Marfatia, Phys. Lett. B **807**, 135579 (2020).
[37] B. Dutta, S. Ghosh, and T. Li, Phys. Rev. D **102**, 055017 (2020).
[38] W. Abdallah, R. Gandhi, and S. Roy, J. High Energy Phys. 12 (2020) 188.
[39] A. Abdullahi, M. Hostert, and S. Pascoli, Phys. Lett. B **820**, 136531 (2021).
[40] J. Liao and D. Marfatia, Phys. Rev. Lett. **117**, 071802 (2016).
[41] M. Carena, Y.-Y. Li, C. S. Machado, P. A. N. Machado, and C. E. M. Wagner, Phys. Rev. D **96**, 095014 (2017).
[42] W. Abdallah, R. Gandhi, and S. Roy, Phys. Rev. D **104**, 055028 (2021).
[43] J. R. Jordan, Y. Kahn, G. Krnjaic, M. Moschella, and J. Spitz, Phys. Rev. Lett. **122**, 081801 (2019).
[44] B. Dutta, D. Kim, A. Thompson, R. T. Thornton, and R. G. Van de Water, Phys. Rev. Lett. **129**, 111803 (2022).
[45] V. Barger, C.-W. Chiang, W.-Y. Keung, and D. Marfatia, Phys. Rev. Lett. **108**, 081802 (2012).
[46] C. E. Carlson and B. C. Rislow, Phys. Rev. D **86**, 035013 (2012).
[47] R. Laha, B. Dasgupta, and J. F. Beacom, Phys. Rev. D **89**, 093025 (2014).
[48] P. Bakhti and Y. Farzan, Phys. Rev. D **95**, 095008 (2017).
[49] W. Altmannshofer, S. Gori, and D. J. Robinson, Phys. Rev. D **101**, 075002 (2020).
[50] G. Krnjaic, G. Marques-Tavares, D. Redigolo, and K. Tobioka, Phys. Rev. Lett. **124**, 041802 (2020).
[51] A. A. Aguilar-Arevalo *et al.* (CCM Collaboration), Phys. Rev. D **107**, 095036 (2023).
[52] B. Dutta, S. Ghosh, and J. Kumar, in Snowmass 2021, arXiv:2203.07786.
[53] K. Kaneta, H.-S. Lee, and S. Yun, Phys. Rev. Lett. **118**, 101802 (2017).
[54] D. Berger, A. Rajaraman, and J. Kumar, Pramana **94**, 133 (2020).
[55] R. N. Pérez, J. E. Amaro, and E. Ruiz Arriola, Phys. Rev. C **95**, 064001 (2017).
[56] J. F. Donoghue and B. R. Holstein, Phys. Rev. D **40**, 2378 (1989).
[57] D. Bryman, P. Depommier, and C. Leroy, Phys. Rep. **88**, 151 (1982).
[58] A. Khodjamirian and D. Wyler, *From Integrable Models to Gauge Theories* (World Scientific, Singapore, 2002).
[59] M. Beneke, V. M. Braun, Y. Ji, and Y.-B. Wei, J. High Energy Phys. 07 (2018) 154.
[60] M. Beneke and J. Rohrwild, Eur. Phys. J. C **71**, 1818 (2011).
[61] A. Bansal and N. Mahajan, Phys. Rev. D **103**, 056017 (2021).
[62] P. Abratenko *et al.* (MicroBooNE Collaboration), Phys. Rev. Lett. **128**, 111801 (2022).
[63] F. Bergsma *et al.*, Phys. Lett. **157B**, 458 (1985).

[64] E. Valencia *et al.* (MINERvA Collaboration), Phys. Rev. D **100**, 092001 (2019).
[65] L. B. Auerbach *et al.* (LSND Collaboration), Phys. Rev. D **63**, 112001 (2001).
[66] L. B. Auerbach *et al.* (LSND Collaboration), Phys. Rev. C **64**, 065501 (2001).
[67] C. Athanassopoulos *et al.* (LSND Collaboration), Phys. Rev. C **58**, 2489 (1998).
[68] B. Armbruster *et al.*, Phys. Lett. B **423**, 15 (1998).
[69] J. Reichenbacher, Final KARMEN results on neutrino oscillations and neutrino nucleus interactions in the energy regime of supernovae, Masters thesis, Karlsruhe Institute of Technology, 2005.
[70] B. Zeitnitz (KARMEN Collaboration), Prog. Part. Nucl. Phys. **32**, 351 (1994).
[71] A. A. Aguilar-Arevalo *et al.* (CCM Collaboration), Phys. Rev. D **106**, 012001 (2022).
[72] A. A. Aguilar-Arevalo *et al.* (CCM Collaboration), Phys. Rev. Lett. **129**, 021801 (2022).
[73] BNL, Liquid argon properties, https://lar.bnl.gov/properties/.
[74] A. Aguilar-Arevalo *et al.* (PIENU Collaboration), Phys. Rev. D **103**, 052006 (2021).
[75] M. Escudero, J. Cosmol. Astropart. Phys. 02 (2019) 007.
[76] D. W. Schmitz, A measurement of hadron production cross sections for the simulation of accelerator neutrino beams and a search for ν_μ to ν_e oscillations in the δm^2 about equals $1 - \mathrm{eV}^2$ region, Ph.D. thesis, Columbisity, 2008.
[77] A. A. Aguilar-Arevalo *et al.* (MiniBooNE Collaboration), Phys. Rev. D **79**, 072002 (2009).